

Limiting mechanisms for photon recycling in thin-film GaAs solar cells

*Original*

Limiting mechanisms for photon recycling in thin-film GaAs solar cells / Gruginskie, N.; Cappelluti, F.; Bauhuis, G.; Tibaldi, A.; Giliberti, G.; Mulder, P.; Vlieg, E.; Schermer, J.. - In: PROGRESS IN PHOTOVOLTAICS. - ISSN 1062-7995. - ELETTRONICO. - 29:3(2021), pp. 379-390. [10.1002/pip.3378]

*Availability:*

This version is available at: 11583/2855893 since: 2020-12-10T13:20:12Z

*Publisher:*

John Wiley and Sons Ltd

*Published*

DOI:10.1002/pip.3378

*Terms of use:*

This article is made available under terms and conditions as specified in the corresponding bibliographic description in the repository

*Publisher copyright*

(Article begins on next page)

RESEARCH ARTICLE

# Limiting mechanisms for photon recycling in thin-film GaAs solar cells

Natasha Gruginskie<sup>1</sup>  | Federica Cappelluti<sup>2</sup>  | Gerard Bauhuis<sup>1</sup> |  
Alberto Tibaldi<sup>2</sup> | Gemma Giliberti<sup>2</sup> | Peter Mulder<sup>1</sup> | Elias Vlieg<sup>1</sup> | John Schermer<sup>1</sup>

<sup>1</sup>Institute for Molecules and Materials, Applied Materials Science, Radboud University, Nijmegen, Netherlands

<sup>2</sup>Department of Electronics and Telecommunications, Politecnico di Torino, Turin, Italy

## Correspondence

Natasha Gruginskie, Institute for Molecules and Materials, Applied Materials Science, Radboud University, Heyendaalseweg 135, Nijmegen 6525 AJ, The Netherlands.  
Email: n.gruginskie@science.ru.nl

## Funding information

Conselho Nacional de Desenvolvimento Científico e Tecnológico, Grant/Award Number: 233259/2014-7; H2020 European Institute of Innovation and Technology, Grant/Award Number: 17043 REGENERATION

## Abstract

Photon recycling mechanisms in single junction thin-film GaAs solar cells are evaluated in this study. Modelling supported by experimentally obtained results is used in order to correlate the reflectance of the cell's rear layers, the photon recycling probability, and the solar cell performance. Solar cells with different top and bottom metalization configurations are produced, and their performance is analyzed from the optical and electrical point of view. It is shown that the photon recycling probability increases with the rear mirror reflectance and solar cell thickness, which results in the increase of the devices open circuit voltage. However, the front grid coverage, usually disregarded in rear mirror focused studies, strongly reduces the photon recycling probability. Furthermore, perimeter and interface recombination hinder the internal radiative efficiency of the solar cells, preventing further increase of the devices' open circuit voltage as a result of improvements of the rear mirror reflectivity. In order to exploit the significant benefit of increased photon recycling probability to the solar cell performance, these limiting mechanisms need to be properly addressed.

## KEYWORDS

GaAs solar cells, photon recycling, thin-film solar cells

## 1 | INTRODUCTION

In the last decade, thin-film single junction GaAs solar cells have surpassed the performance of similar structures processed on the growth substrate, and their world record efficiencies presented an absolute increase of 3%.<sup>1,2</sup> When comparing single junction GaAs solar cells in the thin-film or wafer-based designs, the advantages of the wafer-based architecture are mainly the more mature and quick processing route. The thin-film architecture presents as main advantages the reduced weight and potential of reduced costs with the removal and reuse of the wafer,<sup>3-5</sup> possibility of utilizing thinner epilayers with the

application of a back reflector that increases the light optical path<sup>6-8</sup>; increased resilience to particle irradiation for space application due to the reduced thickness,<sup>9,10</sup> bendability,<sup>11-14</sup> and increased photon recycling due to reflectance of emitted photons.<sup>15-19</sup>

In 2012, Miller et al.<sup>15</sup> showed that, with the application of a high quality back reflector, thin-film GaAs solar cells have the potential to reach efficiencies close to their theoretical limit. In the same study, it was shown that the rear reflectance has a direct impact on the solar cell parameters, most drastically affecting the open circuit voltage ( $V_{oc}$ ), due to a more efficient re-absorption of radiatively emitted photons. Since then, multiple studies have been conducted towards

This is an open access article under the terms of the Creative Commons Attribution-NonCommercial-NoDerivs License, which permits use and distribution in any medium, provided the original work is properly cited, the use is non-commercial and no modifications or adaptations are made.

© 2020 The Authors. Progress in Photovoltaics: Research and Applications published by John Wiley & Sons Ltd

increasing photon recycling in thin-film solar cells, most of which present high quality crystal structures and efficiencies close to 25%.<sup>10,17-24</sup> The main direction is to increase the reflectivity at the rear side, generally resulting in an increase of the devices'  $V_{oc}$ . In most of these studies, however, the achieved  $V_{oc}$  values are well below the expected, often not surpassing 1080 mV.

Initially reported thin-film III-V solar cells typically had highly doped GaAs rear contact layers and fully metallized rear sides.<sup>2,25-28</sup> However, recent studies<sup>19,22</sup> have demonstrated that the reflectance at the rear side of the cells can be significantly increased if the GaAs contact layers are partially removed and replaced by a suitable dielectric layer (such as ZnS) before the final rear side metallization is applied. In this approach, the locally remaining rear-contact areas guarantee a low series resistance contact of the device. The reflectance increases if the rear contact coverage ( $C_r$ ) is reduced and replaced by a superior mirror structure. As a result, the photon recycling increases, showing the onset of the theoretically predicted superlinear increase of  $V_{oc}$ .<sup>15,22</sup> However, for  $C_r = 10\%$  and below, multiple studies reported a strong decrease in the Fill Factor (FF) of the cells due to an increased lateral resistance,<sup>19,22</sup> limiting the possibilities for further efficiency improvement with this approach.

In the present study, the technique to apply a pattern to the rear contact was further elaborated, and working devices with rear side coverage as low as 1.5% were produced. Furthermore, we identify the cause for the shortfall in the achieved  $V_{oc}$ , with respect to the expected value, by evaluating different design strategies for photon recycling based on theoretical modeling and experiments. Using this approach, we demonstrate that for high quality GaAs, it is typically the perimeter and hetero-interface recombination that hinder the

theoretically predicted increase in the open circuit voltage of the cells. If not properly addressed, these limiting mechanisms will prevent the benefits of an optimized rear contact and consequently the possibility to fully exploit the increased photon recycling probability.

## 2 | METHODS

In order to determine the relation between the reflectance of the rear layers of the cells, total photon recycling and device performance, an approach using model simulations combined with experimental analysis of various cell geometries is applied. Firstly, the optical performance of solar cells with different back mirror reflectances are studied, and the probability of photon recycling in these cells is calculated.<sup>17</sup> For that, two solar cell structures, here called structures A and B, with a standard deep-junction (DJ) geometry and GaAs as contact layer are processed into thin-film cells with differently patterned rear contacts. Several aspects are optimized in a third structure, referred to as structure C, aiming to pair the model predictions with the experimental results. Subsequently, an electrical model<sup>16,29,30</sup> is used in order to determine the recombination mechanisms that are dominating the operation of the solar cells.

All solar cell structures used in this study were grown by low-pressure MOCVD on 2 inch diameter GaAs wafers with (1 0 0)  $2^\circ$  off to (1 1 0) orientation. A general schematic depiction of the used solar cell structures and main parameters is shown in Figure 1A, and the various interfaces studied are represented in Figure 1B. All structures have a thick n-doped emitter ( $x_E = 1685$  nm for A and B, and 2000 nm for C), and a thin p-doped base ( $x_B = 100$  nm for all). Two passivating

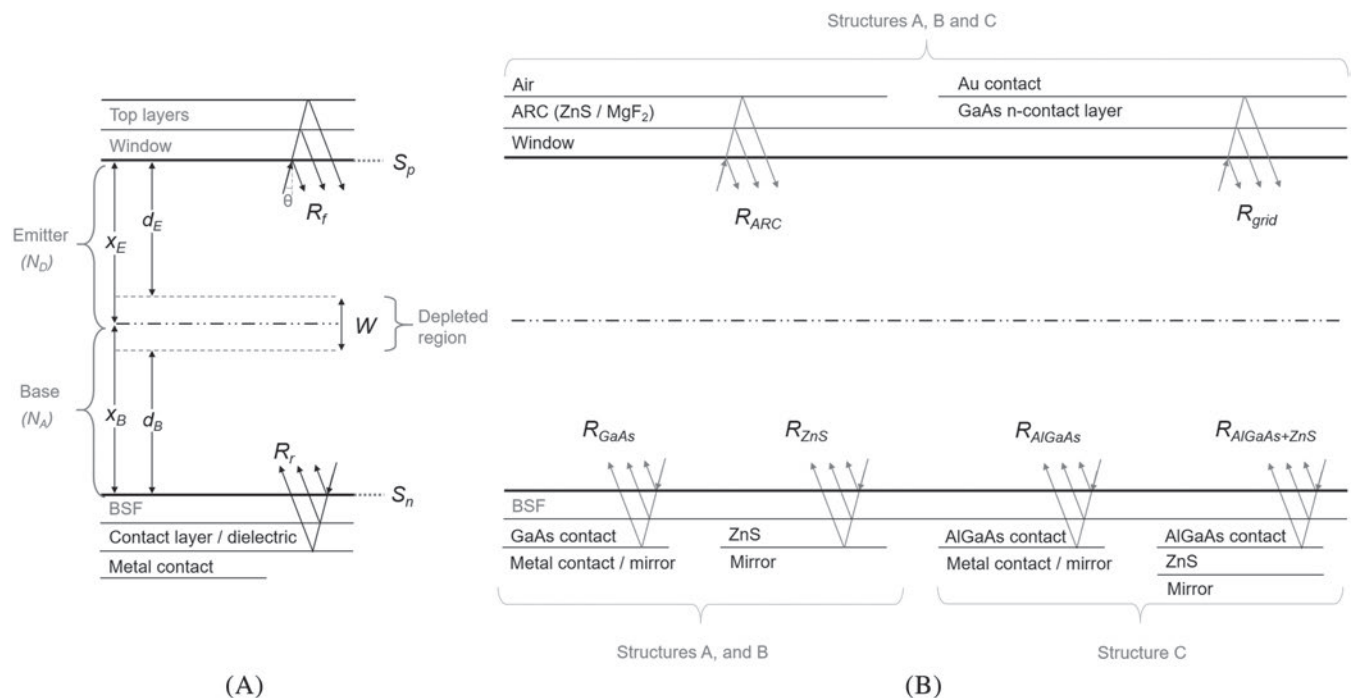


**FIGURE 1** Schematic representation of (A) the solar cell structure and main parameters and (B) the different top and bottom layer structures evaluated in this study

layers, a 20 nm AlInP window and a 100 nm InGaP back surface field (BSF), were grown enclosing the active layers, in order to repel the minority carriers and reduce surface recombination. The outer top and bottom layers of the devices consist of highly doped contact layers that provide low resistance ohmic contact to the metallized parts of the cell. For all structures, the top contact layer consists of 300 nm *n*-GaAs. For the bottom contact layer, 100 nm GaAs was applied for structures A and B, and 150 nm  $\text{Al}_x\text{Ga}_{1-x}\text{As}$  was used for C, with the fraction of Al *x* being 0.1 for the outer 20 nm and 0.3 for the remaining 130 nm. For convenience, this material will be simply referred to as AlGaAs. Details of the layer structures are depicted in Table 1. An AlInGaP etch-stop layer is grown before all solar cell structures in order to stop the etching during the removal of the substrate.

For all structures, the substrate was removed with an aqueous citric acid and hydrogen peroxide solution (5:1 in volume) and the etch-stop layer was removed with HCl 37%. Using photolithography, the resulting 2-inch diameter thin-films had four different patterns applied to the rear side, one for each quadrant for structures A and B, and two different patterns, one for each half of structure C, using a technique described in a previous work.<sup>22</sup> At each film, one section was fully protected with photoresist, that is, the rear surface coverage ( $C_r$ ) is 100%, while the other sections were partly covered using a regular array of 20  $\mu\text{m}$  radius disc-shaped contact points. By varying the pitch distance between the contact points, rear surface coverages between 20% and 1.5% were realized for the different segments of the thin-film samples. Subsequently, for structures A and B the GaAs rear contact layer in between the contact points was etched away using an ammonia:hydrogen peroxide solution and 60 nm of ZnS was thermally evaporated in the etched areas, before the removal of the photoresist. For structure C, the patterning was applied and ZnS was deposited without the removal of the AlGaAs contact layer. The rear side processing of the structures was completed by the removal of the

photoresist and evaporation of a 200 nm thick Au rear contact / mirror layer over the entire surface of all structures and application of copper foils that acts as conductive foreign carrier.

Using e-beam evaporation, the front side of the thin films were equipped with either 200 nm (structures A and B) or 100 nm (structure C) thick Au grid contacts. Subsequently, individual cells were defined by a MESA etch using an ammonia:hydrogen peroxide solution for the GaAs layers and an HBr:Br<sub>2</sub>:H<sub>2</sub>O solution for the phosphide layers. The cells are  $0.5 \times 0.5 \text{ cm}^2$  with a front grid coverage ( $C_f$ ) of 16.6 %. Besides these smaller cells, structure C also includes cells that are  $1.0 \times 1.0 \text{ cm}^2$  with  $C_f = 8\%$ . For all cells, the top *n*-GaAs contact layer in between the grid fingers was removed also using an ammonia:hydrogen peroxide solution. Finally, a thermally evaporated ZnS/MgF<sub>2</sub> (44/94 nm) antireflection coating (ARC) was applied to all cells. Note that the high doping levels of the contact layers allow for low resistivity Ohmic contacts without the need to anneal the thin-film cells. Using the Transfer Length Method (TLM), contact resistivity values were obtained of  $6 \times 10^{-5} \Omega \text{ cm}^2$  for the *p*-AlGaAs contact layer of structure C and  $< 2 \times 10^{-5} \Omega \text{ cm}^2$  for all other (GaAs-based) contact layers.

Illuminated and dark *J* – *V* characterization of the solar cells were performed using an ABET Technologies Sun 2000 Class AAA solar simulator set-up, equipped with a Keithley 2601B source meter, and ReRa Tracer3 software for data acquisition. The solar cells were kept at 25°C during measurement using a heating/cooling water thermostat and a Pt100 temperature sensor. The light intensity was set and corrected using an NREL calibrated reference cell before each measurement series. Because at higher voltages the series resistances cause the dark curve to bend downwards, a set of  $J_{sc} - V_{oc}$  data points measured under different light intensities was used in the dark characteristics analysis, as the series resistance is excluded under these conditions.<sup>31</sup> External Quantum Efficiency (EQE) measurements were performed with a ReRa

**TABLE 1** Layer composition of the epi-layers of the fabricated solar cells

Structure	Layer	Material	Thickness (nm)	Dopant concentration ( $\text{cm}^{-3}$ )	Dopant type
A and B	<i>n</i> -type contact (1)	GaAs	100	$1.3 \times 10^{19}$	Te
	<i>n</i> -type contact (2)	GaAs	200	$5.0 \times 10^{18}$	Si
	Window	AlInP	30	$2.0 \times 10^{17}$	Si
	Emitter	GaAs	1685	$2.0 \times 10^{17}$	Si
	Base	GaAs	100	$1.0 \times 10^{18}$	Zn
	BSF	InGaP	100	$5.0 \times 10^{17}$	Zn
	<i>p</i> -type contact	GaAs	100	$1.0 \times 10^{19}$	Zn
C	<i>n</i> -type contact (1)	GaAs	100	$1.3 \times 10^{19}$	Te
	<i>n</i> -type contact (2)	GaAs	200	$5.0 \times 10^{18}$	Si
	Window	AlInP	30	$2.0 \times 10^{17}$	Si
	Emitter	GaAs	2000	$2.0 \times 10^{17}$	Si
	Base	GaAs	100	$1.0 \times 10^{18}$	Zn
	BSF	InGaP	100	$5.0 \times 10^{17}$	Zn
	<i>p</i> -type contact (1)	$\text{Al}_{0.3}\text{GaAs}$	130	$1.0 \times 10^{18}$	Zn
	<i>p</i> -type contact (2)	$\text{Al}_{0.1}\text{GaAs}$	20	$8.0 \times 10^{18}$	Zn

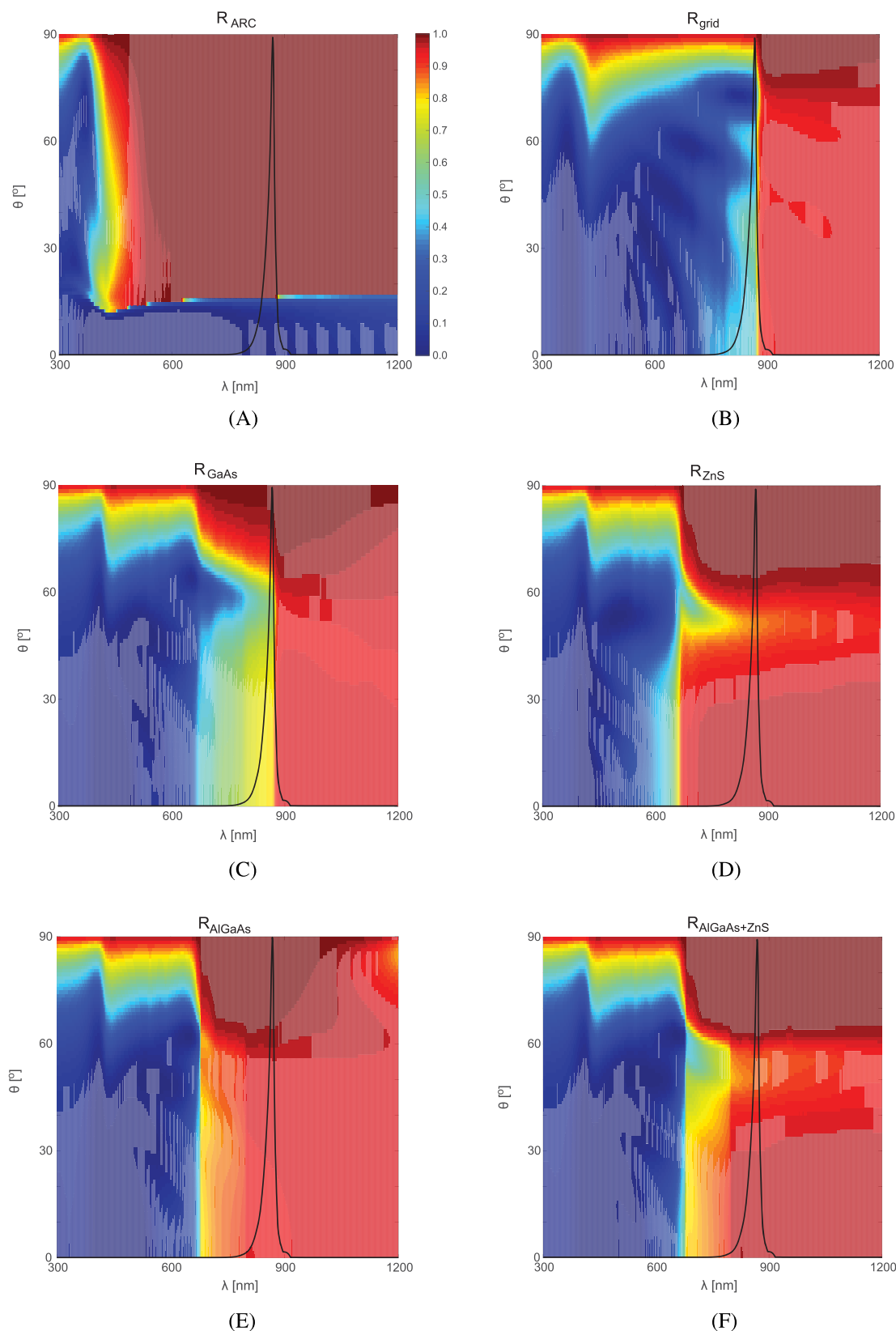


**FIGURE 2** Reflectance maps of the different interfaces evaluated: (A) the internal top reflectance of a region with ARC, (B) the internal top reflectance of a region underneath the metal contacts, and the internal bottom reflectance in solar cells with (C) a 100 nm GaAs contact layer, (D) contact layer replaced with a 60 nm ZnS layer, (E) a 150 nm AlGaAs contact layer, and (F) a 150 nm AlGaAs contact layer with 60 nm ZnS. The reflectance intensity scale is valid for all maps, and the black peak represents the calculated GaAs emission distribution [Colour figure can be viewed at [wileyonlinelibrary.com](http://wileyonlinelibrary.com)]

SpeQuest Quantum Efficiency system. The system uses both a Xenon and Halogen light source to reproduce all the wavelengths present in the solar spectrum, a monochromator to generate quasi-monochromatic light and a chopper for intensity modulation.

The complex refractive index ( $n + ik$ ) required for the theoretical analysis for ZnS,  $\text{MgF}_2$ , AlInP, and InGaP were retrieved from ellipsometry analyses of test samples (typically 100 nm of the material on a GaAs substrate) that were prepared under the same conditions as the corresponding layers in our solar cell structures. These values are available as supplementary information. Reflectance measurements were performed with a FilMetrics spectrophotometer perpendicular to the analyzed surfaces, using a gold mirror for calibration.

A camera with short wavelength infrared detection was used in order to obtain electroluminescence images of the solar cells under externally applied current. The same camera was used to capture images of the solar cells under an inclined angle illumination to visualize the rear contact patterns (no current applied).

### 3 | OPTIMIZED OPTICAL DESIGN

The probability that a photon resulting from radiative recombination is reabsorbed in the active layers of the solar cells is called the photon recycling factor ( $f_{PR}$ ). In the model reported by Steiner et al.,<sup>17</sup>  $f_{PR}$  is averaged for photons emitted spontaneously with emission angles ( $\theta$ ) ranging from  $0^\circ$  to  $90^\circ$ , either upwards or downwards. The model calculates the probability of these photons to reach the interfaces and then be reflected back into the solar cell structure multiple times, with the expression:

$$f_{PR} = 1 - \int_0^\infty \hat{S}(E) \int_0^{\pi/2} \frac{(1 - e^{-\alpha X})}{\alpha X} \left( 1 - \frac{1}{2} \left( 1 - e^{-\alpha X} \right) \left( \frac{R_f + R_r + 2R_f R_r e^{-\frac{\alpha X}{\cos\theta}}}{1 - R_f R_r e^{-\frac{2\alpha X}{\cos\theta}}} \right) \right) \cos\theta \sin\theta d\theta dE, \quad (1)$$

where  $\hat{S}(E)$  represents the normalized spontaneous emission distribution of GaAs,  $\alpha$  is the material's absorption coefficient, and  $X$  is the sum of the emitter and base layers thicknesses ( $x_E + x_B$ ). A similar formulation is also applied to calculate the probability of a radiatively emitted photon to escape through the front surface ( $f_{esc}$ ). By using the optical characteristics of all layers in the solar cell structure, this model implicitly includes the parasitic losses, such as absorption in the non-active layers.

The reflectances at the emitter-window ( $R_f$ ) and at the base-BSF ( $R_r$ ) interfaces of the investigated structures were calculated as a function of photon wavelength (from 300 to 1200 nm) and angle of incidence (from  $0^\circ$  to  $90^\circ$ ) using a 1D coherent optical solver. The optical data of the materials that were not retrieved from ellipsometry measurements were taken from the literature, namely for AlGaAs,<sup>32</sup> GaAs,<sup>33</sup> Ag,<sup>34</sup> and Au.<sup>35</sup>

Figure 2 shows the wavelength ( $\lambda$ ) and angle of incidence ( $\theta$ ) dependent reflectance of the top and bottom interfaces in different

sections of the cells studied in this work (see schematic representation in Figure 1B). For reference, the calculated spontaneous radiative emission distribution of GaAs is also highlighted. For the wavelength range of interest, the front reflectance of the open cell areas ( $R_{ARC}$ , Figure 2A) is high ( $>95\%$ ) for angles of incidence larger than the escape cone ( $\approx 16^\circ$ ), and the low reflectance of light at wavelengths below 500 nm is associated with absorption in the window layer. Underneath the grid contacts, on the other hand, the front reflectance ( $R_{grid}$ , Figure 2B) is considerably lower, due to the high absorption of the  $n$ -GaAs contact layer. Four different structures for the rear interfaces were simulated: a structure containing a 100 nm GaAs contact layer ( $R_{GaAs}$ , Figure 2C), representative of  $C_r = 100\%$ ; a structure from which the contact layer was removed and 60 nm ZnS deposited in its place ( $R_{ZnS}$ , Figure 2D), representative of  $C_r = 0$ ; a structure with a 150 nm AlGaAs as contact layer ( $R_{AlGaAs}$ , Figure 2E); a structure with a 150 nm AlGaAs and 60 nm ZnS deposited on top ( $R_{AlGaAs + ZnS}$ , Figure 2F). All simulated structures have Au as rear contact and/or mirror. For photons in the wavelength range of GaAs spontaneous emission,  $R_{ZnS}$ ,  $R_{AlGaAs}$ , and  $R_{AlGaAs + ZnS}$  are higher than  $R_{GaAs}$  for virtually all angles of incidence. AlGaAs is a material with higher bandgap than GaAs, and therefore does not absorb photons with wavelengths close to that of the GaAs emission. However, the fabrication of AlGaAs layers with doping levels high enough to provide a low ohmic contact resistance without annealing, similar to that of GaAs, is difficult, and therefore not always applied.

The calculated  $f_{PR}$  using Equation (1) for solar cells as a function of  $R_r$  for a range of active layer thicknesses are presented in Figure 3A. In these calculations,  $R_f$  is taken as shown in Figure 2A (disregarding losses in the front contact), and  $R_r$  is considered to be a constant value, independent of photon energy or angle of incidence. For cells with a perfect mirror ( $R_r = 100\%$ ), all radiative losses represent photons being absorbed in or escaping through the front layers. Thicker devices are less dependent on the reflectances of the interfaces, as denoted by their less steep curve. This highlights the importance of an optimized optical design in the development of thin and ultra-thin solar cells.<sup>6,9,28</sup>

In order to estimate the total photon recycling factor of the studied solar cells, the  $f_{PR}$  was initially calculated for each rear interface separately, considering  $R_f$  of both the open cell areas ( $f_{PR(ARC)}$ ), and the solar cell regions underneath the grid ( $f_{PR(grid)}$ ). Subsequently, the photon recycling of devices with a single rear mirror structure ( $f_{PR(R_r)}$ ) is determined taking the front grid into account by:

$$f_{PR(R_r)} = C_f \times f_{PR(grid)} + (1 - C_f) \times f_{PR(ARC)}, \quad (2)$$

calculated separately for the different rear mirror configuration. For the patterned solar cells, the resulting photon recycling factor ( $f_{PR(device)}$ ) is considered to be the weighted average of the  $f_{PR(R_r)}$  of the different regions making up the cell structures. Therefore:

$$f_{PR(device)} = C_r \times f_{PR(GaAs)} + (1 - C_r) \times f_{PR(ZnS)}, \quad (3a)$$

for cells from epi-structures A and B, or

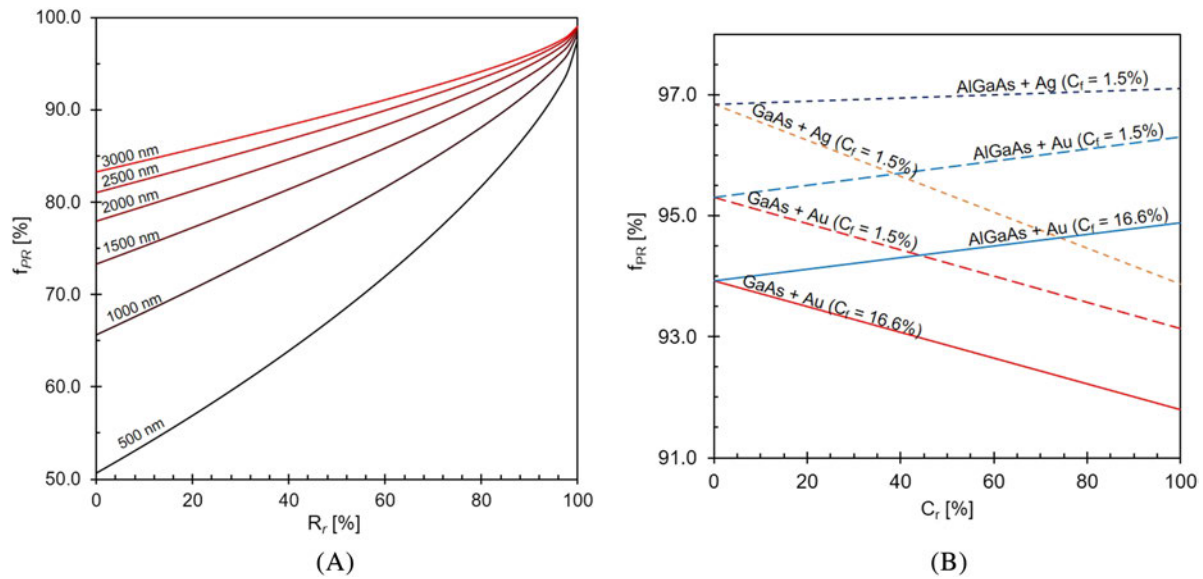


**FIGURE 3** Photon recycling factor as a function of (A) the rear contact reflectivity for solar cells with different active layer thicknesses and (B) the rear contact coverage of solar cells with different materials for  $p$ -contact layer and mirror [Colour figure can be viewed at [wileyonlinelibrary.com](http://wileyonlinelibrary.com)]

$$f_{PR(\text{device})} = C_r \times f_{PR(\text{AlGaAs})} + (1 - C_r) \times f_{PR(\text{AlGaAs} + \text{ZnS})}, \quad (3b)$$

for cells from epi-structure C.

Figure 3B depicts  $f_{PR}$  as a function of  $C_r$ , calculated as in Equations (2) and (3a), with the thickness of the active layers of structures A and B. Two different front configurations are considered for the determination of  $R_f$ : the applied grid with  $C_f = 16.6\%$  (solid lines) and an optimized low front contact coverage of  $C_f = 1.5\%$  (dashed lines). It is shown that, for the epi-structures A and B (red lines), the maximum  $f_{PR}$  to be reached with low coverage front contacts and Au rear contact is of 95.3%, approximately 2.2% absolute increase as compared to the non-patterned cells ( $C_r = 100\%$ ). For the cells with  $C_f = 16.6\%$ , there is an overall reduction in photon recycling of  $\approx 1.4\%$  absolute, identifying the front contact grid coverage as an important limiting factor to the cells optical quality. Furthermore, higher photon recycling values can theoretically be obtained by applying other metals or contact layer materials, as it is also depicted in the picture for the case of AlGaAs as rear contact layer (blue lines) and Ag as rear contact and/or mirror.

Interestingly, according to these calculations, the patterning does not improve the photon recycling factor of solar cells with AlGaAs as contact layer, and in fact it decreases up to  $\approx 1.0\%$  points for  $C_r = 0$  as compared to  $C_r = 100\%$ . The main reason for that is that ZnS is moderately absorbing at higher angles of incidence, as can be seen in the reflectance map of Figure 2C, and in more detail for  $\lambda = 870$  nm in Figure 4. Although  $R_{\text{ZnS}}$  and  $R_{\text{AlGaAs} + \text{ZnS}}$  are higher than  $R_{\text{AlGaAs}}$  for normal incident photons, they are lower when averaged for all angles of incidence, and therefore  $f_{PR}$  decreases with the patterning.

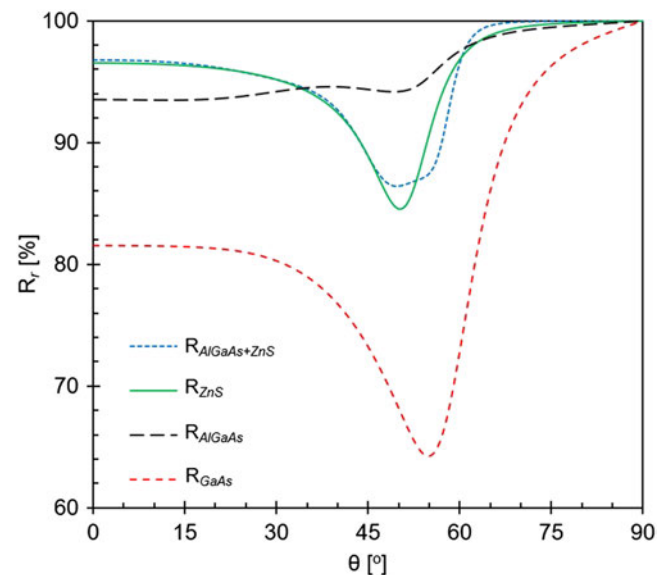


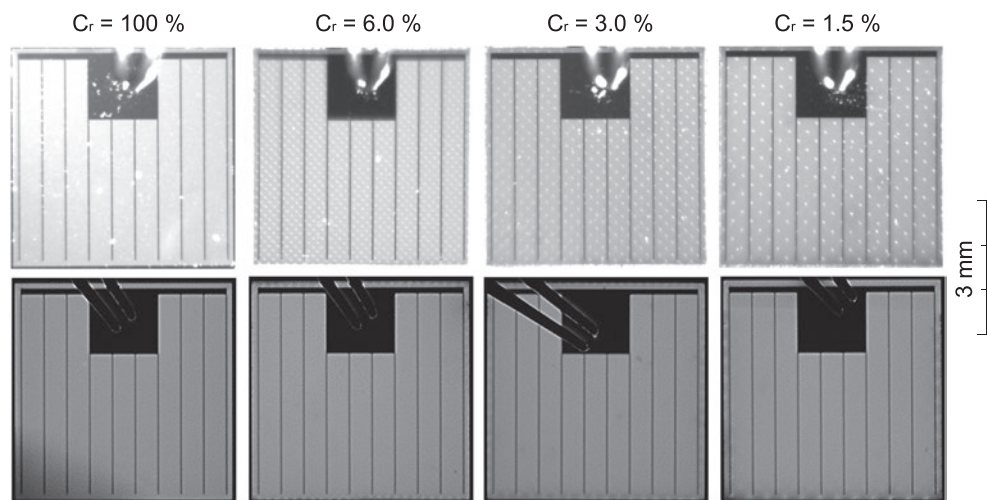
**FIGURE 4** Calculated angle-dependent reflectance of the four studied bottom layer structures for  $\lambda = 870$  nm [Colour figure can be viewed at [wileyonlinelibrary.com](http://wileyonlinelibrary.com)]

## 4 | RESULTS AND DISCUSSION

In order to circumvent the limitation of previously reported rear contact patterning approaches,<sup>19,22</sup> a smaller pattern for the rear contact consisting of  $20 \mu\text{m}$  radius discs was developed and applied to the rear of solar cells from epi-structures A and B. In this manner, the distance between contact spots was reduced significantly, as shown in the photographs of Figure 5, allowing the production of cells with very low  $C_r$ .



**FIGURE 5** Inclined illumination (top row) and electroluminescence (bottom row) images of the solar cells from structure B with different  $C_r$ . The applied current for the electroluminescence images and camera settings were kept the same for each series of measurement



In the photographs taken under inclined illumination (top row of Figure 5), it is possible to visualize the contact spots, which are hard to be observed in the electroluminescence images (bottom row of Figure 5) due to the small distance between them. The illuminated  $J-V$  parameters of the best performing cells from structures A and B, as shown in Table 2, indicate that applying these small radius contact points the FF of the cells do not show a sudden large drop at  $C_r = 10\%$ .<sup>19,22</sup> Even for cells with  $C_r$  as low as 3% the FF is only less than 1% point lower than for the reference cells ( $C_r = 100\%$ ), while for the more extreme case of  $C_r = 1.5\%$  the FF is less than 3% points lower.

Based on the modeling results, cells from epi-structures C were designed to strengthen the photon recycling mechanisms. Therefore, they were fabricated with a thicker emitter and using AlGaAs as rear contact layer. Moreover, in order to reduce the perimeter recombination, the devices produced from structure C included cells with a larger area ( $1.0 \times 1.0 \text{ cm}^2$ ), yielding a reduced front coverage of  $C_f = 8\%$ . The increased cell size reduces the number of cells that can be produced from this epi-structure, and therefore only two rear

contact patterns were applied to the structure, with  $C_r = 100\%$  and  $C_r = 10\%$ . Since the simulations show negligible difference between  $R_{\text{ZnS}}$  and  $R_{\text{AlGaAs + ZnS}}$  in the wavelength range of GaAs emission, the produced solar cells from epi-structure C had ZnS locally deposited on top of the contact layer, as opposed to replacing it, in order to avoid an unnecessary etching step.

The measured specular reflectance of the two  $1.0 \times 1.0 \text{ cm}^2$  cells processed from structure C are shown in Figure 6. For the light with wavelength just above the GaAs band cut-off, the patterning (i.e., local rear contacting) in fact increases the reflectance at normal incidence. However, the illuminated  $J-V$  parameters from these cells, summarized in Table 2, show that, as expected from the photon recycling calculations, the  $V_{oc}$  values of both cells are quite similar, confirming that there is no optical benefit in applying a pattern to the

**TABLE 2** Illuminated  $J-V$  parameters of the best cells of each configuration

	$C_r$ [%]	$V_{oc}$ (mV)	$J_{sc}$ (mA/cm <sup>2</sup> )	FF (%)	$\eta$ (%)
Structure A	100	1058.8	23.1	85.0	21.0
	20	1063.5	23.1	84.4	20.8
	15	1068.4	23.6	84.3	21.3
	10	1069.7	23.4	84.6	21.3
Structure B	100	1062.2	23.0	84.5	20.6
	6.0	1067.3	23.3	84.1	20.7
	3.0	1069.5	23.2	84.0	20.8
	1.5	1071.0	23.7	82.2	20.8
Structure C	100	1073.8	25.2	82.1	22.2
$0.5 \times 0.5 \text{ cm}^2$	10	1074.8	25.8	85.4	23.7
Structure C	100	1078.0	28.0	72.6	21.9
$1.0 \times 1.0 \text{ cm}^2$	10	1076.7	28.0	75.4	22.8

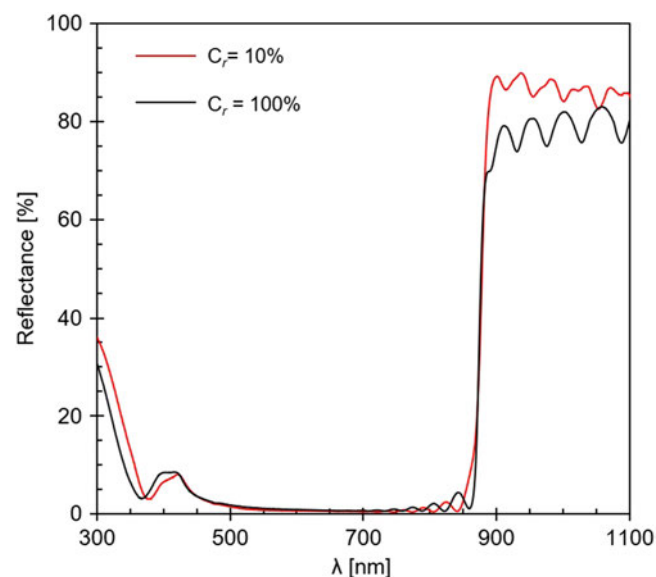


**FIGURE 6** Measured reflectance at normal incidence for solar cells produced from epi-structure C [Colour figure can be viewed at [wileyonlinelibrary.com](http://wileyonlinelibrary.com)]



rear contact. It is worth noticing that the devices present a much lower fill factor (FF) than the smaller  $0.5 \times 0.5 \text{ cm}^2$  cells from structures A, B, and C indicating that the reduced front grid coverage has become a limiting factor in the efficiencies of these cells. To compensate for this a thicker front grid metallization is required.

The expected open circuit voltage of the produced cells can be calculated according to:<sup>15</sup>

$$V_{oc} = V_{db} + \frac{kT}{q} \ln(\eta_{ext}), \quad (4)$$

where  $V_{db}$  is the detailed balance limit voltage and  $\eta_{ext}$  is the external radiative efficiency. In order to predict the open circuit voltage of the solar cells due to deliberate changes in the rear mirror design, the external radiation efficiency is calculated as:<sup>17</sup>

$$\eta_{ext} = \frac{\eta_{int} f_{esc}}{1 - \eta_{int} f_{PR}}, \quad (5)$$

where  $\eta_{int}$  is the internal radiative efficiency, defined as the fraction of all recombination events in the solar cell that takes place radiatively. While  $f_{PR}$  and  $f_{esc}$  can be easily calculated using the optical data of the device materials,  $\eta_{int}$  is related to the overall quality of the solar cells and varies greatly depending on growth and processing conditions. Using constant values for  $V_{db} = 1.145 \text{ V}$ <sup>17,23</sup> and for  $f_{esc} = 1.08\%$  (which is the average of the cells from structures A and B),  $V_{oc}$  as a function of  $f_{PR}$  is calculated for a range of  $\eta_{int}$  values, and shown in Figure 7.

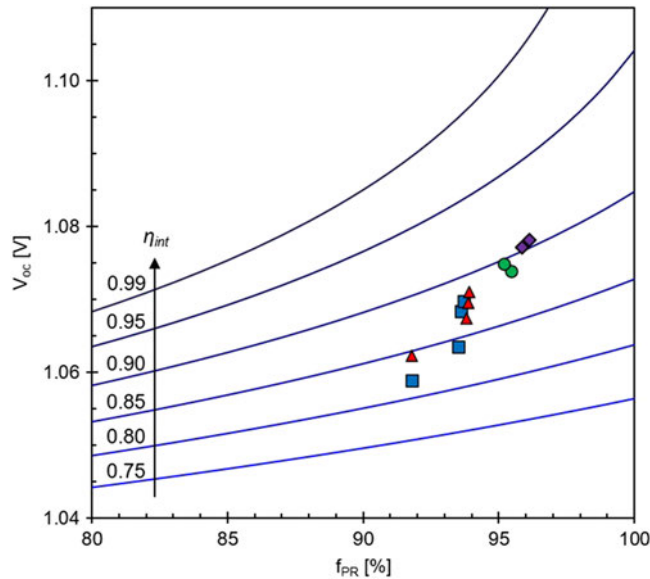


**FIGURE 7** Open circuit voltage as a function of the photon recycling factor for different internal radiative efficiency values. The markers represent the  $V_{oc}$  values related to their calculated  $f_{PR}$ , for the  $0.5 \times 0.5 \text{ cm}^2$  cells from structures A (blue squares), B (red triangles) and C (green circles), and the  $1.0 \times 1.0 \text{ cm}^2$  cells from structure C (purple diamonds) [Colour figure can be viewed at [wileyonlinelibrary.com](http://wileyonlinelibrary.com)]

For a first order comparison, the experimental  $V_{oc}$  values of cells fabricated from the epi-structures A, B, and C together with their calculated  $f_{PR}$  values are also included in Figure 7. Even though the theoretical trend neglects the slight variations of  $V_{db}$  and  $f_{esc}$  for the different structures, the comparison with the experimental data provides a good indication of the range of the devices internal radiative efficiency. Most of these cells have  $\eta_{int}$  values in between 80% and 90%, which means that, aside from rear mirror reflectance, there are other aspects that need to be optimized in order to take advantage of the  $V_{oc}$  enhancement offered by photon recycling.

The analysis of the solar cells dark curves allows us to gauge the overall quality of the devices. Solar cells in the dark under forward bias are generally analyzed as two diodes in parallel, expressed by:

$$J_{dark} = J_{01} \left( e^{\frac{q(V+J_{R_s})}{kT}} - 1 \right) + J_{02} \left( e^{\frac{q(V+J_{R_s})}{2kT}} - 1 \right) + \frac{V + J_{R_s}}{R_{sh}}, \quad (6)$$

where  $J_{01}$  and  $J_{02}$  are the saturation current densities of the  $1kT$  and  $2kT$  components, respectively. In this equation,  $q$  is the electron charge,  $k$  is the Boltzmann constant,  $T$  is the temperature, and  $R_{sh}$  and  $R_s$  are the parasitic shunt and series resistances, respectively. The evaluated solar cells have sufficiently large  $R_{sh}$  (at least  $1 \times 10^8 \Omega \text{ cm}^2$ ) so there is no visible effect in the dark curves, and therefore the term  $(V + J_{R_s})/R_{sh}$  can be disregarded. The possible effects of  $R_s$  in the curves are circumvented by the use of  $J_{sc} - V_{oc}$  data under different light intensities. The extracted parameters from the fit of Equation (6) to the measured dark curves for the different cell geometries are shown in Table 3.

$J_{02}$  represents the nonradiative recombination that takes place predominantly in the space charge region ( $J_{0,SCR}$ ) and at the perimeter ( $J_{0,perim}$ ) of the cell and is given as  $J_{02} = J_{0,SCR} + J_{0,perim}$ , with  $J_{0,SCR}$  estimated as:

$$J_{0,SCR} = \frac{qWn_i^2}{\sqrt{\epsilon_p \epsilon_n}}. \quad (7)$$

**TABLE 3** Dark  $J - V$  parameters of the best cells of each configuration

	$C_r$ (%)	$J_{01}$ (A/cm <sup>2</sup> )	$J_{02}$ (A/cm <sup>2</sup> )
Structure A	100	$3.8 \times 10^{-20}$	$8.5 \times 10^{-12}$
	20	$3.2 \times 10^{-20}$	$9.0 \times 10^{-12}$
	15	$3.0 \times 10^{-20}$	$9.9 \times 10^{-12}$
	10	$2.5 \times 10^{-20}$	$6.5 \times 10^{-12}$
Structure B	100	$4.5 \times 10^{-20}$	$1.1 \times 10^{-11}$
	6.0	$2.3 \times 10^{-20}$	$5.4 \times 10^{-12}$
	3.0	$1.9 \times 10^{-20}$	$1.3 \times 10^{-11}$
	1.5	$2.0 \times 10^{-20}$	$6.4 \times 10^{-12}$
Structure C	100	$3.2 \times 10^{-20}$	$1.0 \times 10^{-11}$
	$0.5 \times 0.5 \text{ cm}^2$	$3.5 \times 10^{-20}$	$1.2 \times 10^{-11}$
	100	$2.6 \times 10^{-20}$	$2.1 \times 10^{-12}$
	$1.0 \times 1.0 \text{ cm}^2$	$2.7 \times 10^{-20}$	$1.8 \times 10^{-12}$

At higher voltages, on the other hand, the dark curve is dominated by  $J_{01}$ , which arises from the recombination of minority carriers in the quasi neutral regions (QNR) and at the front and rear interfaces.<sup>36–38</sup> For cells where defect-assisted recombination is negligible, and carriers diffusion length is much larger than the QNRs thickness, that is, bulk recombination is negligible with respect to the surface recombination,  $J_{01}$  can be approximated as the sum of a surface-limited diffusion component ( $J_{0,diff}$ ) and a radiative recombination component ( $J_{0,rad}$ ) given as:<sup>30</sup>

$$J_{0,diff} = \frac{qD_p n_i^2}{N_D} \frac{S_p}{S_p d_E + D_p} + \frac{qD_n n_i^2}{N_A} \frac{S_n}{S_n d_B + D_n}, \quad (8a)$$

and

$$J_{0,rad} = q(x_E + x_B) n_i^2 B (1 - f_{PR}). \quad (8b)$$

The diffusion coefficient  $D_{p(n)}$  of the devices were calculated according to the empirical model described by Sotoodeh et al.,<sup>29</sup> and the minority carriers' lifetimes  $\tau_p$  and  $\tau_n$  were defined as:<sup>16</sup>

$$\frac{1}{\tau_{p(n)}} = \frac{1 - f_{PR}}{\tau_{p(n),rad}} + \frac{1}{\tau_{p(n),SRH}}, \quad (9)$$

where the subscripts *rad* and *SRH* indicate the radiative and Shockley-Read-Hall recombination lifetimes, respectively. SRH lifetime is estimated according to the doping-dependent empirical model from Lumb et al.,<sup>16</sup> while radiative lifetime is defined as  $\tau_{p(n),rad} = 1/BN_{D(A)}$ , with  $N_{D(A)}$  being the emitter (base) doping. For thermodynamic consistency, the radiative recombination rate coefficient  $B$  was calculated by integrating the spontaneous emission rate associated with the GaAs optical data used in the other calculations and is found to be  $6.22 \times 10^{-10}$  cm<sup>3</sup>/s. The use of these theoretical lifetimes and mobilities provides a good match to the solar cells external quantum efficiencies. The top and bottom interface recombination velocities ( $S_p$  and  $S_n$ , respectively) in Equation (8a) are fitted based on the experimentally extracted  $J_{01}$ . For cells with the DJ geometry, the dark current is found to be largely influenced by small changes in  $S_p$ , while it is less sensitive to changes in  $S_n$ . Therefore,  $S_n$  is considered to be similar to  $S_p$ , and the same values are used in the model for both recombination velocities.

The perimeter recombination fraction is generally not computed in dark curve analysis, but it can account for a large fraction of the dark current of small solar cells, such as the cells applied in CPV systems and the here studied  $0.5 \times 0.5$  cm<sup>2</sup> devices, for which the perimeter-to-area ratio (P/A) is large.<sup>38,39</sup> In contrast to the other saturation current densities,  $J_{0,perim}$ , is difficult to predict, since it can vary largely as a function of the quality of the technique that defines the solar cell area (such as the used MESA etchants). In large area cells, however,  $J_{02}$  is likely to be mostly limited by  $J_{0,SCR}$ .

The expected increase in photon recycling due to the increased rear reflectance of the solar cells will only reduce  $J_{0,rad}$  (and therefore reduce  $J_{01}$ ). In Table 3, it is shown that, while there is a consistent decrease in  $J_{01}$  with the reduction of  $C_r$  for the cells with structures A

and B, there is no significant difference between the dark parameters of the two rear side configurations from structure C, confirming the small variation of  $f_{PR}$  for these samples. The difference in  $J_{01}$  observed between the different sized cells from structure C is due to the increase in  $f_{PR}$  granted by the reduced  $C_f$  in the  $1.0 \times 1.0$  cm<sup>2</sup> cells.  $J_{0,diff}$ , on the other hand, is limited by the quality of the hetero-interfaces,<sup>10,30</sup> so in order to fully benefit from the increase in photon recycling, it is important that  $J_{0,rad}$  dominates the dark curve at  $V \approx V_{oc}$ , and therefore  $J_{0,diff}$  and  $J_{0,perim}$  should be as low as possible.

The dark characteristics components of the  $0.5 \times 0.5$  cm<sup>2</sup> solar cells with  $C_r = 100\%$  from epi-structures B and C are shown in Figure 8A,B, respectively. These curves show that, in both structures,  $J_{0,perim}$  is much higher than  $J_{0,SCR}$ , dominating the dark curve at lower voltages. Furthermore,  $J_{0,diff}$  is larger than  $J_{0,rad}$  even for the cells with  $C_r = 100\%$ , due to  $S_p$  and  $S_n$  values of approximately  $4 \times 10^3$  cm/s. This indicates that the interface and perimeter recombination are limiting the  $\eta_{int}$  value of these solar cells, and need to be addressed for a successful production of high efficiency devices. The modeled dark curve of the  $1.0 \times 1.0$  cm<sup>2</sup> cell with AlGaAs contact layer (epi-structure C) with  $C_r = 100\%$  is shown in Figure 8C. The  $J_{02}$  values are lower for these cells than for the  $0.5 \times 0.5$  cm<sup>2</sup> cells, as a result of the lower impact of the perimeter recombination on the device performance, which is clearly visible in Figure 8C. Though lower, also for the  $1.0 \times 1.0$  cm<sup>2</sup> cells  $J_{0,perim}$  is higher than  $J_{0,SCR}$ , indicating that the performance of the devices would benefit from applying a passivation technique.<sup>40,41</sup>

Also for the  $1.0 \times 1.0$  cm<sup>2</sup> cells from structure C,  $J_{0,diff} > J_{0,rad}$ , but  $J_{0,rad}$  is slightly lower than for the cells from structures A and B, due to the higher photon recycling factor. The fact that  $S_{p(n)}$  is comparable ( $\approx 4 \times 10^3$  cm/s) in all fabricated structures causes all the structures to have similar  $J_{0,diff}$ , and therefore, despite the increased  $f_{PR}$  of samples from structure C, the decrease in  $J_{01}$  is small. The nonnegligible  $S_{p(n)}$  values indicate a suboptimal passivation from the window and BSF layers, most likely due to a lower epi-layer quality at the hetero-interfaces, as recently addressed in the literature.<sup>42–45</sup> A meticulous control of chemical composition, material inter-diffusion, and surface segregation is necessary in order to prevent the formation of mixed compounds that reduce the abruptness of the interfaces.

A theoretical example of dark curve from a thin-film solar cell in which  $J_{perim}$  and  $J_{diff}$  are not limiting the dark characteristics is shown in Figure 8D. This curve demonstrates the potential performance of cells from epi-structure C processed with very low P/A and with an effective passivation provided by the window and BSF layers. In this example,  $J_{0,perim}$  is set to  $1 \times 10^{-13}$  A/cm<sup>2</sup> and  $S_{p(n)} = 100$  cm/s, resulting in an approximated  $J_{01}$  of  $5 \times 10^{-21}$  A/cm<sup>2</sup>. The expected  $J_{0,diff}$  for this structure is much lower than  $J_{0,rad}$ , which results in a larger sensitivity of the dark curve to changes in the photon recycling factor. Therefore, it becomes clear that fine tuning the growth conditions of the hetero-interfaces, and therefore, achieving high quality interface passivation is one of the most important guidelines towards the fabrication of solar cells that can fully benefit from an efficient photon recycling. Furthermore, for applications such as concentration systems, in which cells are often required to have small dimensions, the

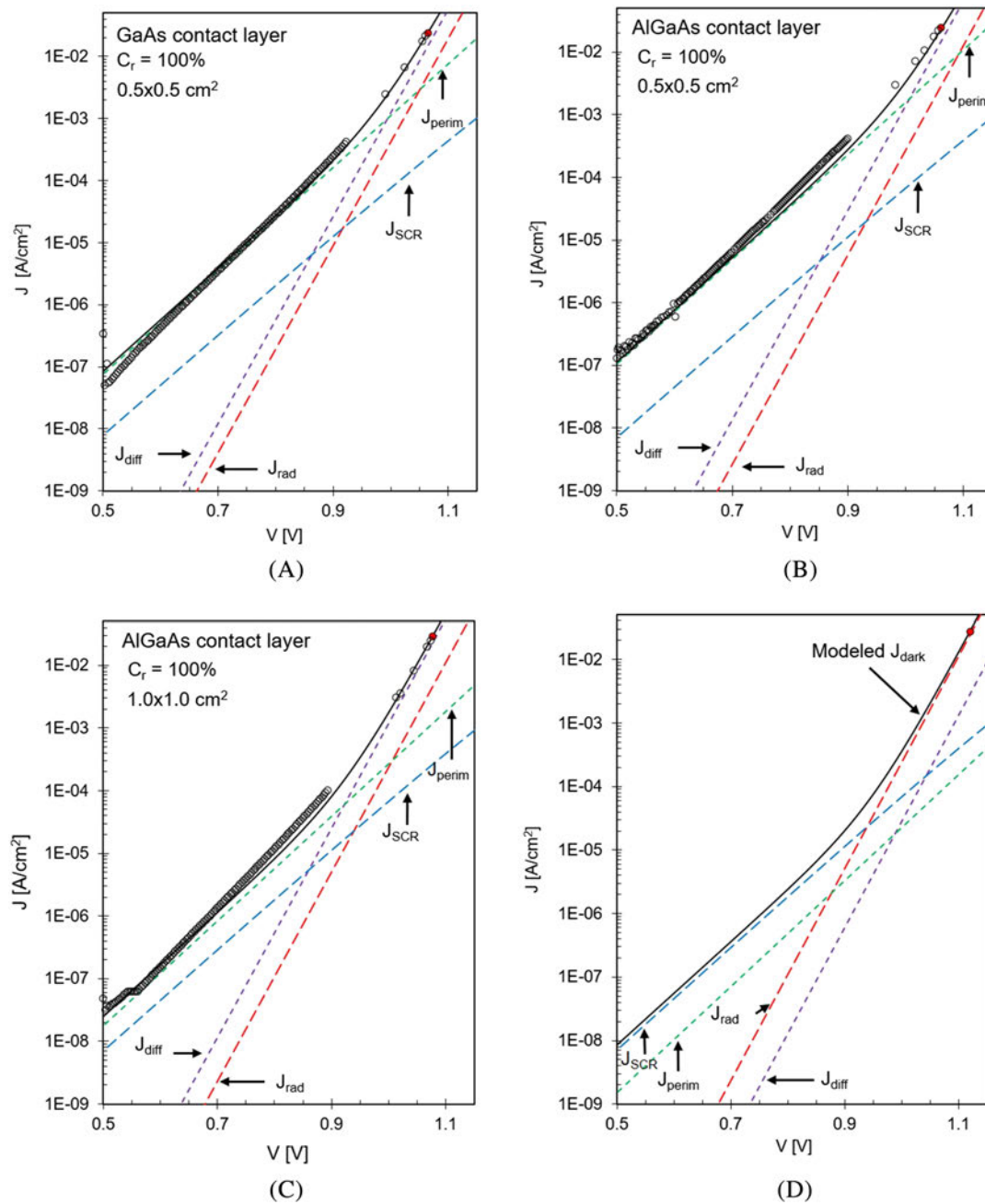


**FIGURE 8** Experimental (markers) and modeled (solid line) dark characteristics of (A) a  $0.5 \times 0.5 \text{ cm}^2$  thin-film solar cell with GaAs as contact layer ( $C_r = 100\%$ ), (B) a  $0.5 \times 0.5 \text{ cm}^2$  thin-film solar cell with AlGaAs as contact layer ( $C_r = 100\%$ ), (C) a  $1.0 \times 1.0 \text{ cm}^2$  thin-film solar cell with AlGaAs as contact layer ( $C_r = 100\%$ ), and (D) an example of dark curve representative of a thin-film solar cell with high quality hetero-interfaces and small P/A. The curves are modeled as the sum of the diffusion ( $J_{\text{diff}}$ , purple), radiative ( $J_{\text{rad}}$ , red), perimeter ( $J_{\text{perim}}$ , green) and space charge region ( $J_{\text{SCR}}$ , blue) recombination current densities. The red markers in (A), (B), and (C) represent the  $J_{\text{sc}}$  and  $V_{\text{oc}}$  values under AM1.5G illumination, and in (D), it represents the expected  $V_{\text{oc}}$  at a similar  $J_{\text{sc}}$  to sample C [Colour figure can be viewed at [wileyonlinelibrary.com](http://wileyonlinelibrary.com)]

use of a perimeter passivation technique must be considered in order to overcome the limitations imposed by perimeter recombination.

The expected electrical performance from a solar cell as depicted in Figure 8D is shown in Figure 9 (solid red lines), excluding the effect of parasitic resistances. It is shown that, by attenuating the effects of interface and perimeter recombination from the  $1.0 \times 1.0 \text{ cm}^2$  cell with structure C, a maximum  $V_{\text{oc}} = 1.095 \text{ V}$  can be achieved. By

further improving the cells optical design, with the application of a front grid with  $C_f = 1.5\%$  and Ag back contacts, the curves shown as dashed lines in Figure 9 can be expected. These two simulated structures differ mainly in  $f_{\text{PR}}$ , and the optical improvements applied to structure C do not alter the absorption of light by the semiconductor, as observed by the minor difference between the two simulated EQE curves. The superior  $J_{\text{sc}}$  obtained by the structure with improved

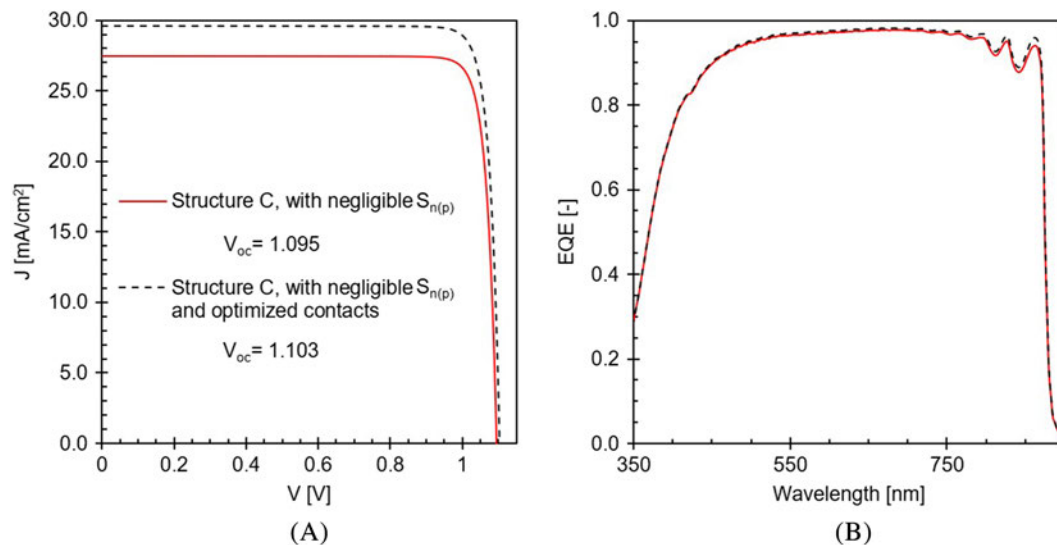


**FIGURE 9** Modeled (A) illuminated J-V and (B) EQE curves of cells from epi-structure C ( $C_f = 8\%$ ) with very low P/A and an effective passivation provided by the window and BSF layers (solid red lines). The dashed black lines represent the same structures with minimized front grid ( $C_f = 1.5\%$ ) and Ag used as rear mirror/contact [Colour figure can be viewed at [wileyonlinelibrary.com](http://wileyonlinelibrary.com)]

contacts is, therefore, mainly due to the reduced shadow losses on the front grid. By applying these suggested design changes to the cells of this particular structure, a maximum  $V_{oc} = 1.103$  V can be achieved.

## 5 | CONCLUSIONS

The present study further develops a technique of patterning the bottom contact layer of single junction thin-film GaAs solar cells previously shown in the literature, and the reported sudden decrease in FF for rear coverages lower than 10% is no longer observed. The production of functional devices with rear contact coverages as low as 1.5% was achieved, and the produced cells show a direct correlation between total bottom reflectance and solar cell performance.

With the rear contact no longer limiting the cells efficiency, it was possible to pinpoint the performance limiting mechanisms of these solar cells. Using optical and electrical modelling, it was demonstrated that the front grid coverage, usually disregarded in rear mirror focused studies, considerably reduces the photon recycling probability, and therefore limits the maximum open circuit voltage that the devices can achieve. This effect can be attenuated by applying a minimal front grid coverage or, more suitably for small cell areas, by reducing the thickness of the front contact layer.

Furthermore, perimeter and interface recombination were identified as limiting factors for the internal radiative efficiency of the solar cells, preventing further increase of the open circuit voltage as a result of improvements to the rear mirror reflectance. The perimeter recombination contribution to the dark current can be reduced by the production of larger area cells, but for the devices with  $P/A = 4 \text{ cm}^{-1}$  evaluated in this study,  $J_{\text{perim}}$  is still dominating the dark curve at lower voltages. In addition, a reduction of at least one order of magnitude of the surface recombination velocity at the front and rear interfaces is

required in order to sufficiently decrease the surface recombination dark current component, enabling a significant benefit of increased photon recycling probability to the solar cell performance. If the effects of perimeter and interface recombination are minimized, and optimized front and back contacts are applied, an open circuit voltage of 1.103 V can be achieved by solar cells with the specific structure used in this study.

## ACKNOWLEDGEMENTS

The authors acknowledge financial support from the Brazilian National Council for Scientific and Technological Development (CNPq), under the program Science Without Border, project number 233259/2014-7, and funding under grant agreement 17043 REGENERATION from the European institute for Innovation and Technology (EIT), a body supported by the European Union's Horizon 2020 research and innovation program.

## ORCID

Natasha Gruginskie  <https://orcid.org/0000-0001-6571-0538>

Federica Cappelluti  <https://orcid.org/0000-0003-4485-9055>

## REFERENCES

- Green MA, Dunlop ED, Hohl-Ebinger J, Yoshita M, Kopidakis N, Ho-Baillie AWY. Solar cell efficiency tables (Version 55). *Prog Photovolt Res Appl*. 2019;27:3-15.
- Bauhuis GJ, Mulder P, Haverkamp EJ, Huijben JCCM, Schermer JJ. 26.1% thin-film GaAs solar cell using epitaxial lift-off. *Sol Energy Mater Sol Cells*. 2009;93(9):1488-1491.
- Voncken MMAJ, Schermer JJ, Bauhuis GJ, Mulder P, Larsen PK. Multiple release layer study of the intrinsic lateral etch rate of the epitaxial lift-off process. *Appl Phys Mater Sci Process*. 2004;79(7):1801-1807.
- Bauhuis GJ, Mulder P, Haverkamp EJ, et al. Wafer reuse for repeated growth of III-V solar cells. *Prog Photovolt Res Appl*. 2010;18(3):155-159.

5. Adams J, Elarde V, Hains A, et al. Demonstration of multiple substrate reuses for inverted metamorphic solar cells. In: 2012 IEEE 38th Photovoltaic Specialists Conference (PVSC) Part 2; 2012:1-6.
6. van Eerden M, Bauhuis G, Mulder P, et al. A facile light trapping approach for ultra-thin GaAs solar cells using wet chemical etching. *Prog Photovolt Res Appl*. 2020;28:200-209.
7. Bauhuis GJ, Schermer JJ, Mulder P, Voncken MMAJ, Larsen PK. Thin film GaAs solar cells with increased quantum efficiency due to light reflection. *Sol Energy Mater Sol Cells*. 2004;83(1):81-90.
8. Cappelluti F, Ghione G, Gioannini M, et al. Novel concepts for high-efficiency lightweight space solar cells. *E3S Web Conf*. 2017;16:03007.
9. Hirst LC, Yakes MK, Warner JH, et al. Intrinsic radiation tolerance of ultra-thin GaAs solar cells. *Appl Phys Lett*. 2016;109(3):033908.
10. Gruginskie N, Cappelluti F, Bauhuis G, et al. Electron radiation induced degradation of GaAs solar cells with different architectures. *Prog Photovolt Res Appl*. 2020;28:266-278.
11. Stender CL, Adams J, Elarde V, et al. Flexible and lightweight epitaxial lift-off GaAs multi-junction solar cells for portable power and UAV applications. In: 2015 IEEE 42nd Photovoltaic Specialist Conference, PVSC 2015; 2015:8-11.
12. Feenstra J, Leest RHV, Smeenk NJ, et al. Flexible shielding layers for solar cells in space applications. *J Appl Polym Sci*. 2016;133:43661.
13. Moon S, Kim K, Kim Y, Heo J, Lee J. Highly efficient single-junction GaAs thin-film solar cell on flexible substrate. *Sci Report*. 2016;6:1-6.
14. Kwak P, Kim N, Kim J, Kim D, Song K, Lee J. Flexible space solar cell array with radiation shield fabricated by guided-printing of cover glasses. *Sol Energy Mater Sol Cells*. 2017;169:210-214.
15. Miller OD, Yablonovitch E, Kurtz SR. Intense internal and external fluorescence as solar cell approach the SQ efficiency limit. *Photovoltaics, IEEE J*. 2012;2(3):1-27.
16. Lumb MP, Steiner MA, Geisz JF, Walters RJ. Incorporating photon recycling into the analytical drift-diffusion model of high efficiency solar cells. *J Appl Phys*. 2014;116(19):194504.
17. Steiner MA, Geisz JF, García I, Friedman DJ, Duda A, Kurtz SR. Optical enhancement of the open-circuit voltage in high quality GaAs solar cells. *J Appl Phys*. 2013;113:123109.
18. Hwang ST, Kim S, Cheun H, et al. Bandgap grading and Al<sub>0.3</sub>Ga<sub>0.7</sub>As heterojunction emitter for highly efficient GaAs-based solar cells. *Sol Energy Mater Sol Cells*. 2016;155:264-272.
19. Hwang S-T, Hwang T, Lee S, Gil B, Park B. Selective rear contact for Ga<sub>0.5</sub>In<sub>0.5</sub>P- and GaAs- based solar cells. *Sol Energy Mater Sol Cells*. 2018;182:348-353.
20. Kosten ED, Kayes BM, Atwater HA. Experimental demonstration of enhanced photon recycling in angle-restricted GaAs solar cells. *Energ Environ Sci*. 2014;7(6):1907-1912.
21. Walker AW, Höhn O, Micha DN, Bläsi B, Bett AW, Dimroth F. Impact of Photon Recycling on GaAs Solar Cell Designs. *IEEE J Photovoltaics*. 2015;5:1636-1645.
22. Gruginskie N, van Laar SCW, Bauhuis G, et al. Increased performance of thin-film GaAs solar cells by rear contact/mirror patterning. *Thin Solid Films*. 2018;660:10-18.
23. Micha DN, Hohn O, Oliva E, Bett AW, Dimroth F. Development of back side technology for light trapping and photon recycling in GaAs solar cells. *Prog Photovolt Res Appl*. 2019;27:163-170.
24. Schilling CL, Höhn O, Micha DN, et al. Combining photon recycling and concentrated illumination in a GaAs heterojunction solar cell. *IEEE J Photovoltaics*. 2018;8(1):348-354.
25. Schemer JJ, Mulder P, Bauhuis GJ, Larsen PK, Oomen G, Bongers E. Thin-film GaAs epitaxial lift-off solar cells for space applications. *Prog Photovolt Res Appl*. 2005;13(7):587-596.
26. Schermer JJ, Bauhuis GJ, Mulder P, et al. Photon confinement in high-efficiency, thin-film III-V solar cells obtained by epitaxial lift-off. *Thin Solid Films*. 2006;511-512:645-653.
27. Yoon J, Jo S, Chun IS, et al. GaAs photovoltaics and optoelectronics using releasable multilayer epitaxial assemblies. *Nature*. 2010;465:329-33.
28. Vandamme N, Chen HL, Gaucher A, et al. Ultrathin GaAs solar cells with a silver back mirror. *IEEE J Photovoltaics*. 2015;5(2):565-570.
29. Sotoodeh M, Khalid AH, Rezazadeh AA. Empirical low-field mobility model for III-V compounds applicable in device simulation codes. *J Appl Phys*. 2000;87(6):2890-2900.
30. Sun Y, Perna A, Bermel P. Comparing front- and rear-junction GaInP photovoltaic devices through detailed numerical and analytical modeling. *IEEE J Photovoltaics*. 2019;9(2):437-445.
31. Bauhuis G, Mulder P, Hu YY, Schermer J. Deep junction III-V solar cells with enhanced performance. *Phys Status Solidi (A) Appl Mater Sci*. 2016;213(8):2216-2222.
32. Adachi S. GaAs, AlAs and Al<sub>x</sub>Ga<sub>1-x</sub>As: Materials parameters for use in research and device applications. *J Appl Physiol*. 1985;58(3):1-29.
33. Palik ED. *Handbook of Optical Constants of Solids*. Vol 3. Cambridge, Massachusetts: Academic Press; 1998.
34. Jiang Y, Pillai S, Green MA. *Realistic silver optical constants for plasmonics*. 2016;6:30605.
35. Sopra n-k database. <http://www.sspectra.com/sopra.html>
36. Hovel HJ. *Semiconductors and Semimetals*, Vol. II: Solar cells. New York: Academic Press; 1975.
37. Nelson J. *The Physics of Solar Cells*. London: Imperial College Press; 2003.
38. Ochoa M, Algora C, Espinet-González P, García I. 3-D modeling of perimeter recombination in GaAs diodes and its influence on concentrator solar cells. *Sol Energy Mater Sol Cells*. 2014;120:48-58.
39. Espinet-González P, Rey-Stolle I, Ochoa M, Algora C, García I, Barrigón E. Analysis of perimeter recombination in the subcells of GaInP / GaAs / Ge triple-junction solar cells. *Prog Photovolt: Res Appl*. 2015;23:874-882.
40. Sandroff CJ, Nottenburg RN, Bischoff JC, Bhat R. Dramatic enhancement in the gain of a GaAs/AlGaAs heterostructure bipolar transistor by surface chemical passivation. *Appl Phys Lett*. 1987;51(1):33-35.
41. Sheldon MT, Eisler CN, Atwater HA. GaAs passivation with tri-octylphosphine sulfide for enhanced solar cell efficiency and durability. *Adv Energy Mater*. 2012;2(3):339-344.
42. Nakano T, Shioda T, Enomoto N, et al. Precise structure control of GaAs/InGaP hetero-interfaces using metal organic vapor phase epitaxy and its abruptness analyzed by STEM. *J Cryst Growth*. 2012;347(1):25-30.
43. Fukushima Y, Nakano T, Nakano Y, Shimogaki Y. Control of in surface segregation and inter-diffusion in GaAs on InGaP grown by metal-organic vapor phase epitaxy. *Jpn J Appl Phys*. 2012;51:055601.
44. Wells NP, Driskell TU, Hudson AI, et al. Carrier quenching in InGaP / GaAs double heterostructures. *J Appl Phys*. 2015;118:065703.
45. López-escalante MC, Gabás M, García I, Barrigón E, Rey-stolle I, Algora C. Applied surface science differences between GaAs / GaInP and GaAs / AlInP interfaces grown by MOVPE revealed by depth profiling and angle-resolved X-ray photoelectron spectroscopies. *Appl Surf Sci*. 2016;360:477-484.

**How to cite this article:** Gruginskie N, Cappelluti F, Bauhuis G, et al. Limiting mechanisms for photon recycling in thin-film GaAs solar cells. *Prog Photovolt Res Appl*. 2020;1-12. <https://doi.org/10.1002/pip.3378>